

Dewetting of liquid film via vapour-mediated Marangoni effect

Seungho Kim^{1,2}, Joonoh Kim¹ and Ho-Young Kim^{1,†}

¹Department of Mechanical and Aerospace Engineering, Seoul National University, Seoul 08826, Korea

²Department of Biological and Environmental Engineering, Cornell University, Ithaca, NY 14853, USA

(Received 4 September 2018; revised 11 March 2019; accepted 5 May 2019)

Liquid films on wettable solid surfaces can be disturbed to dewet when low surface tension liquids or surfactants are added because the surface tension difference gives rise to stresses on the film interface. Here we consider an alcohol drop placed above a thin aqueous film, which punctures a hole in the film starting from underneath the alcohol drop. Such film dewetting is attributed to the Marangoni effects caused by the spatial gradient of alcohol vapour concentration. We measure the liquid–gas interfacial tension of aqueous liquids rapidly responding to the surrounding isopropyl alcohol vapour concentration, and observe evolution of the film morphology consisting of central hole, fringe film, thinning region and bulk. We construct scaling laws to predict the dewetting rates of the film by considering the Marangoni stress, viscous shear stress and evaporation. It is shown that our experiments are consistent with our theory.

Key words: capillary flows, contact lines, thin films

1. Introduction

Thin liquid films on non-wettable surfaces easily dewet when subjected to small disturbances, while they are relatively stable on wettable surfaces (Keller 1983; Redon, Brochard-Wyart & Rondelez 1991; Kim, Moon & Kim 2013). Besides a mechanical scheme to blow an airflow through a narrow nozzle (Berendsen *et al.* 2012), adding a low surface tension liquid drop on the film was found to cause film dewetting (Gaver & Grotberg 1990; Troian, Herbolzheimer & Safran 1990; Jensen & Grotberg 1992; Warner, Craster & Matar 2004; Hernández-Sánchez, Eddi & Snoeijer 2015) or even fragmentation (Keiser *et al.* 2017) on a wettable solid. This is owing to the difference of the interfacial tensions of the two liquids, which develops the stress at the liquid surface pointing radially outward. While the drop merely spreads out on a liquid pool of sufficient depth (Berg 2009; Kim *et al.* 2017), the outward radial flow nucleates a hole in thin liquid films to expose a dry solid surface.

Here we consider a liquid film placed under a volatile low surface tension droplet. The film on a highly wettable solid is punctured underneath the droplet (Marra & Huethorst 1991), implying that one can remotely induce the dewetting of a liquid without direct mixing of multiple liquids. Such interfacial phenomena are attributed to

† Email address for correspondence: hyk@snu.ac.kr

the Marangoni effect caused by the spatial gradient of organic vapour concentration, which we term the vapour-mediated Marangoni effect. This effect was previously explored in order to dry water films on substrates that are withdrawn from a water bath by supplying organic vapour near the water–air–solid contact line (Leenaars, Huethorst & van Oekel 1990). Although such a Marangoni drying process of wet surfaces was numerically analysed (Matar & Craster 2001), the growth dynamics of a dry hole and the complicated thickness variation of the water film under the effects of organic vapour have yet to be addressed.

Interfacial flows driven by the vapour-mediated Marangoni effect were also observed in the motion of liquid drops. Bangham & Saweris (1938) found that a water drop could be moved by an adjacent acetone drop. The motion was supposed to be caused by a thin invisible film emitted from the acetone drop that changed the solid–gas interfacial tension around the water drop. Carles & Cazabat (1989) reported a relatively volatile trans-decaline (TD) drop to repel a polydimethylsiloxane (PDMS) drop. The TD vapour condensed on the PDMS drop was supposed to reduce the liquid–gas interfacial tension locally, inducing the Marangoni flows and eventually displacing the entire drop. Cira, Benusiglio & Prakash (2015) proposed a mechanism to explain the relative motion of two compound drops, in which the vapour from each drop was supposed to affect the liquid–gas interfacial tension of the other drop's precursor films.

The specific goals of this study are as follows. First, we aim to evaluate the effects of isopropyl alcohol (IPA) vapour on the instantaneous surface tension of aqueous liquids. This is because the previous studies of vapour-mediated drop motion mostly relied on speculation of the effects of the vapours without quantitative data of the surface tension coefficient as a function of the vapour concentration. Second, we aim to provide theoretical models to rationalize the dynamic behaviour of film profiles, which is based on the aforementioned measurement of surface tension. The fundamental understanding of the mechanisms underpinning the film dewetting behaviours owing to the vapour-mediated Marangoni effect will open a novel pathway to control the shape, motion and evaporation of liquid films.

In the following sections, we start by measuring the instantaneous change of liquid–gas interfacial tension of aqueous liquids as a function of the concentration of surrounding IPA vapour. Then we observe the shape evolution of a thin liquid film on a highly wettable solid surface owing to IPA vapour in the atmosphere. As the film dewets, rich interfacial dynamics are observed including recession of fringe film with growth of a dry hole, emergence of a very thin region connecting the fringe and the bulk, and recession of a bulk rim. We theoretically analyse the flows and construct scaling laws to predict the evolution rate of each region.

2. Experiments

2.1. Measurement of liquid–gas interfacial tension

To measure the instantaneous change of liquid–gas interfacial tension under the effects of surrounding IPA vapour, we use the pendant drop method as schematically shown in figure 1(a). A drop of liquid emerges from the lower end of a vertically situated capillary tube with inner radius $a = 0.58$ mm. As a liquid, we use deionized water and aqueous glycerine solutions of 30 wt% and 60 wt%. Table 1 lists the physical properties of the liquids used in the experiments. We make the inner wall of the glass tube highly wettable by cleaning it with the piranha solution, i.e. a 3:1 mixture of sulphuric acid and 30% hydrogen peroxide solution. The shape of the drop is such



FIGURE 1. (a) A schematic of the experimental apparatus to measure the liquid–gas interfacial tension at different concentrations of IPA vapour. (b) Images of a swelling water drop as the IPA vapour concentration increases with time. The distance of the IPA source to the liquid drop, s , and the initial liquid column height, l , are 20 and 35 mm, respectively.

	Liquid	ρ (kg m ⁻³)	γ_0 (N m ⁻¹)	μ (Pa s)
A	Water	998	0.072	0.001
B	Glycerine 30 wt%	1071	0.069	0.0022
C	Glycerine 60 wt%	1151	0.067	0.009

TABLE 1. Properties of liquids used in experiments.

that the hydrostatic pressure at the bottom of the tube, $\Delta p_h = \rho g l$ with ρ being the density of liquid, g the gravitational acceleration and l the height of liquid column, is balanced by the Laplace pressure, i.e. a product of the drop curvature and the liquid–gas interfacial tension γ_{LG} . By measuring the liquid column height and the curvature, we deduce γ_{LG} .

The measurement takes place in an acrylic vessel equipped with a shutter at the bottom under which a pool of IPA is contained. The 17 cm high vessel has a square cross-section measuring 10×10 cm², and is open to the atmosphere at the top. Upon placing the liquid-filled tube above the bath of IPA, we open the shutter to let the IPA vapour diffuse into the air inside the vessel. As the concentration of IPA molecules surrounding the liquid drop increases with time, it swells as shown in figure 1(b), indicating the decrease of γ_{LG} . The shape of the meniscus $z = z(r)$ is related to γ_{LG} via the Young–Laplace equation

$$\frac{d^2 z}{dr^2} + \frac{1}{r} \frac{dz}{dr} \left[1 + \left(\frac{dz}{dr} \right)^2 \right] = \frac{\rho g}{\gamma_{LG}} (l + b - l_J - z) \left[1 + \left(\frac{dz}{dr} \right)^2 \right]^{3/2}, \quad (2.1)$$

where l_J is the Jurin height, or the equilibrium capillary rise height of the uncontaminated liquid with the liquid–gas interfacial tension γ_0 and zero contact angle $l_J = 2\gamma_0 / (\rho g)$, and b is the distance between the tube bottom and the drop apex, as shown in figure 1(a). One can solve (2.1) numerically under such boundary conditions as $z = dz/dr = 0$ at $r = 0$ with an assumed value of γ_{LG} . The computational results are compared with the experimental images of the liquid drop to improve the guess of γ_{LG} , which eventually gives γ_{LG} . We see good agreement of the experimentally found liquid–gas interfacial profile and the numerical result with a correctly assumed γ_{LG} in figure 2(a).

Figure 2(b) shows the measurement results of the temporal evolution of the surface tension coefficient of the liquid drops at different distances from the source, s . The

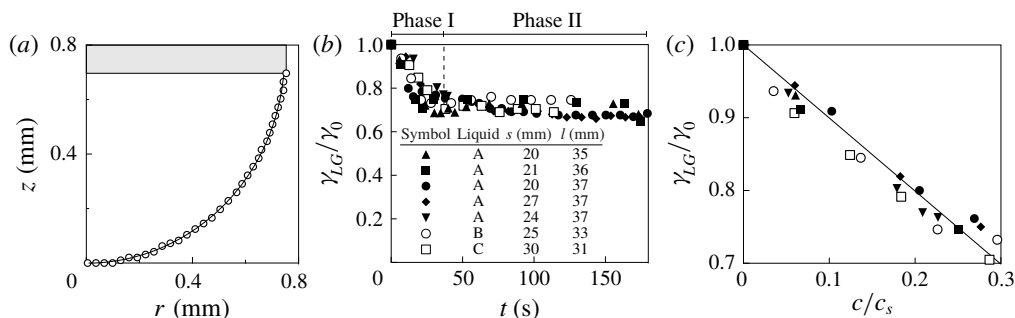


FIGURE 2. (a) Meniscus profile of an IPA-contaminated water drop with $\gamma_{LG} = 0.050 \text{ N m}^{-1}$. The circles and solid line correspond to the experimental results and the solution of the Young–Laplace equation (2.1), respectively. (b) The scaled liquid–gas interfacial tension γ_{LG}/γ_0 versus time. (c) Re-plotting the data of γ_{LG}/γ_0 , which correspond to the instantaneous response of surface tension to the IPA vapour in phase I, versus c/c_s .

scaled surface tension γ_{LG}/γ_0 decreases for initial ~ 20 s (phase I) and then it plateaus (phase II). The change of the surface tension is related to the IPA vapour concentration in the air, c , which obeys the one-dimensional diffusion equation with the boundary conditions being such that $c = c_s$ at the surface of IPA pool ($s = 0$) and $c = 0$ as $s \rightarrow \infty$ as follows

$$c = c_s \operatorname{erfc} \left(\frac{s}{2\sqrt{Dt}} \right). \quad (2.2)$$

Here, $c_s = 142 \text{ g m}^{-3}$ and $D = 1 \times 10^{-5} \text{ m}^2 \text{ s}^{-1}$ (Lugg 1968) are the saturation concentration and the diffusion coefficient of IPA in the air at 25°C , respectively. The surface tension coefficient of water with volumetric mixing of liquid IPA was measured (Hernández-Sánchez *et al.* 2015), which showed monotonic decrease of the surface tension with the increase of the volumetric composition of IPA. However, considering that c increases monotonically with time in the current experiments, the surface tension data of the volumetric mixture of water and liquid IPA are not likely to explain the plateau in figure 2(b).

We carry out additional experiments to scrutinize the effects of the IPA vapour on the surface tension, in which we suddenly remove the IPA vapour in air by closing the shutter and supplying fresh air in the vessel. When the removal occurs in phase I (at 10 s), the pendant drop almost recovers its original shape but at a lower rate than when γ_{LG} is being lowered, as shown in figure 9(a). This indicates a profound effect of the IPA vapour concentration in the surrounding air on the surface tension of the liquid in phase I.

As discussed in appendix A, in the early stages of the exposure of an aqueous liquid surface to IPA vapour, the adsorption of IPA vapour molecules to the liquid surface is supposed to play a dominant role in altering the surface tension of the liquid. Therefore, it is the IPA vapour concentration in the surrounding air, not the volumetric composition of IPA in the water-IPA mixture, that determines the surface tension of liquid in phase I. Here, phase I refers to the initial period when the surface tension is decreased under a low concentration of IPA vapour in the surrounding air ($c/c_s < 0.2$). We see that the rather scattered data of γ_{LG}/γ_0 are collapsed onto a single line when plotted versus c/c_s in figure 2(c), implying a dominant effect of the IPA

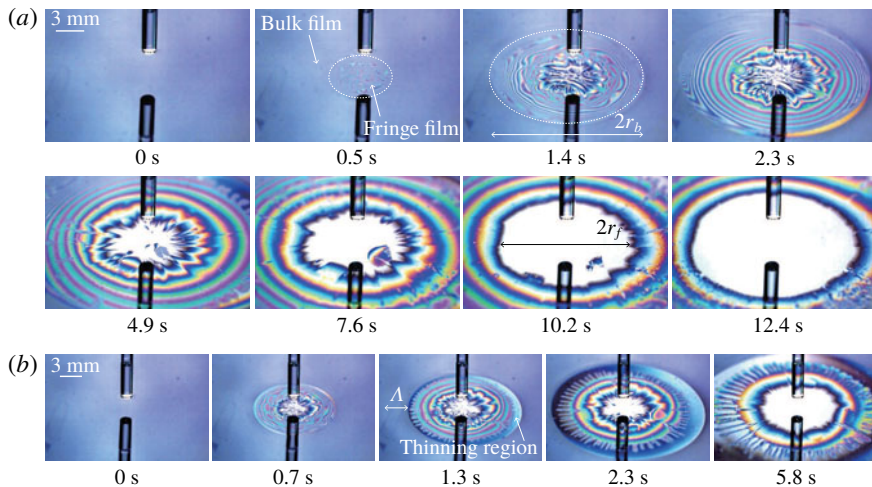


FIGURE 3. (Colour online) IPA vapour-induced dewetting of water films with the original thickness, h_0 , of (a) $30\ \mu\text{m}$ and (b) $50\ \mu\text{m}$.

vapour concentration on surface tension in phase I. In the following experiments of dewetting films, fresh surfaces are continually generated, whose instantaneous surface tension under the effects of IPA vapour is assumed to follow the behaviour exhibited in phase I.

2.2. Observations of film dewetting

To observe the dynamics of a liquid film under the effects of IPA vapour, we prepare a highly hydrophilic surface in the following procedure. We immerse a 10 cm diameter silicon wafer in the piranha solution for 1 h. Upon withdrawing the wafer from the solution, we rinse it with deionized water. The wafer is dried with nitrogen gas and then treated with oxygen plasma for 5 min. To obtain a thin film on the circular wafer, we place liquid drops on the wafer and horizontally vibrate it until the entire circular area is covered with a thin film. The resulting film is almost free from interference patterns owing to its flatness as shown in the first images (0 s) of figures 3(a) and 3(b). The film thickness, h_0 , is deduced from its weight measured by a precision balance (Mettler Toledo XS205). The resolution of the balance is 0.1 mg, which corresponds to the uncertainty range of $\pm 0.01\ \mu\text{m}$ in deducing the film thickness. Special care is taken to keep the wafer surface horizontal and free from contamination, failure of which results in notably abnormal film dewetting behaviours including elliptic dry holes and locally pinned contact lines.

A capillary tube is filled with IPA to its Jurin height, $l_j \approx 1\ \text{cm}$ with $a = 0.58\ \text{mm}$. This forms a meniscus of zero curvature at the lower end of the tube, allowing us to neglect the effects of interface curvature on the vapour pressure of IPA (Butt, Graf & Kappl 2006). We slowly bring the capillary tube from $\sim 3\ \text{cm}$ to a distance d above the film, which takes approximately $\tau_0 = 10\ \text{s}$. The time t is measured since the tube reaches the final position at d . The dynamics of the liquid film is imaged by a CMOS camera (Photron SA 1.1) at a frame rate of $60\ \text{s}^{-1}$ with a resolution of 896×896 pixels. Figure 3 shows the responses of liquid films to IPA vapour emitted from the capillary tube.

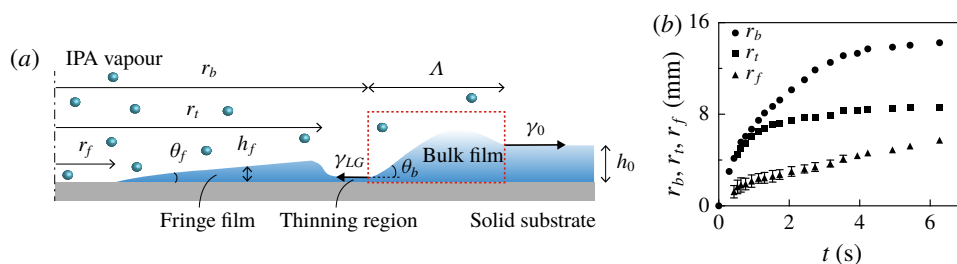


FIGURE 4. (Colour online) (a) Thickness profile of a dewetting film. (b) Temporal evolution of the inner radii of bulk film r_b , thinning region r_t , and fringe film r_f . The original thickness of the water film was $h_0 = 50 \mu\text{m}$, and the IPA source was $d = 2 \text{ mm}$ above the film.

For a film of $h_0 = 30 \mu\text{m}$, figure 3(a), we observe the reduction of film thickness below the IPA source, indicating the recession of bulk from the centre. The growing region of reduced thickness is enclosed by a dotted line ($t = 0.5$ and 1.4 s). The physical origin of the bulk recession is simple – the high concentration of IPA molecules adsorbed on the water surface in the centre lowers the liquid–gas interfacial tension locally. Then the peripheral area with a relatively high surface tension draws the liquid away from the region of a high IPA concentration, causing the bulk to recede from the centre. The continual decrease of the thickness eventually punctures the film ($t > 2.3 \text{ s}$). The retraction of a fringe film right next to the dry area is unstable and thus forms fingers ($t = 2.3$ and 4.9 s), which are diminished as the dry hole keeps expanding ($t > 7.6 \text{ s}$).

Figure 3(b) for a thicker film with $h_0 = 50 \mu\text{m}$ exhibits a narrower area of reduced thickness compared with figure 3(a), which allows us to see a thickness profile of the film from the central dry area to the peripheral bulk area in one image (1.3 and 2.3 s). The image at $t = 1.3 \text{ s}$ clearly shows that the surrounding bulk area and an inner area developing fingers is separated by an annulus of very small thickness. It is indicated as a thinning region, being thinner than both its inner and outer regions.

Therefore, we schematically draw the thickness profile of the film from the centre to periphery as in figure 4(a). The dry region meets the fringe film at a distance r_f from the centre, and the fringe film is surrounded by the thinning region at r_t . Thus, r_f and r_t correspond to the inner radii of the fringe film and the thinning region, respectively. We note that the average radius of the dry hole was used to obtain the value of r_f when fingers were developed. The thinning region ends at r_b , where the bulk begins. The film thickness reaches h_0 after bulging to form a ridge of characteristic length Λ . Figure 4(b) plots the growth of r_f , r_t , and r_b with the continual supply of IPA vapour from the source.

3. Theoretical analysis

3.1. Receding of bulk

We first consider the rate of bulk receding, or the growth of r_b . The Reynolds number based on the characteristic receding speed \dot{r}_b , and the film height h_0 , $Re = \rho \dot{r}_b h_0 / \mu$, is less than 1 for all the cases. Furthermore, the product of Re and the aspect ratio h_0 / r_b is less than 10^{-1} , and thus we neglect inertia as compared with viscous forces (Batchelor 1967). The flow is driven by the difference in the liquid–gas interfacial

tensions across the ridge of the characteristic width Λ , $\Delta\gamma_{LG} \sim 10^{-2} \text{ N m}^{-1}$. The gravitational effects are negligible because the Bond number $Bo = \rho g h_0^2 / \Delta\gamma_{LG} \sim 10^{-2}$. The balance of the driving interfacial forces and the resisting viscous forces gives the receding rate of the bulk, or $r_b(t)$.

Because $h_0 \ll r_b$ for most of the dewetting process, we ignore the curvature effects and consider a simple force balance for a dotted control volume in figure 4(a). The liquid–gas interfacial tension in the periphery beyond the ridge is assumed to be close to that of the uncontaminated liquid, γ_0 , because of continual replenishing flow in the bulk. The liquid–gas interfacial tension at the outer rim of the thinning region, $r = r_b$, is lower than γ_0 because the IPA molecules adsorbed on the thinning region are hardly advected to the surrounding for the small thickness of the region. The surface tension coefficient γ_{LG} varies with the distance from the IPA source and time, and thus the driving force $\Delta\gamma = \gamma_0 - \gamma_{LG}$ changes as the bulk recedes, which we evaluate in the following paragraph.

As γ_{LG} is a function of IPA concentration c as shown in figure 2(b), we first consider c on a film at a distance $(r_b^2 + d^2)^{1/2}$ from the IPA source. Adopting the solution for diffusion in the spherical coordinates from a source of radius a (Carslaw & Jaeger 1959), we estimate $c/c_s \approx (a/r_b) \text{erfc}(1/2r_b/\sqrt{D\tau})$, where we used $(r_b^2 + d^2)^{1/2} \approx r_b$ for $d \ll r_b$. Here $\tau \approx \tau_0 + t$ is the duration the water film is exposed to IPA, as explained in § 2.2. We have $\tau \gg 1/4r_b^2/D \sim 1 \text{ s}$, and thus $c/c_s \approx a/r_b$. When c/c_s is small for $a/r_b \ll 1$, the data in figure 2(c) allows us to approximate $\gamma_{LG}/\gamma_0 \approx 1 - \xi c/c_s$ with $\xi \approx 1$. Therefore, the liquid–gas interfacial tension at r_b is scaled as $\gamma_{LG}/\gamma_0 \sim 1 - a/r_b$, which gives the driving force per unit depth $\Delta\gamma \sim \gamma_0 a/r_b$.

The viscous resisting force per unit depth, F_r , associated with flows in the ridge can be estimated using the well known inertialess wedge flow assumption (de Gennes 1985; Redon *et al.* 1991; Kim, Lee & Kang 2002; Kim 2007). By solving the Stokes equation and integrating the wall shear stress in the ridge, one obtains $F_r \sim \mu \dot{r}_b \ln(\Lambda/h_t)/\theta_b$, where h_t is the thickness of the thinning region and θ_b is taken to be a constant of 0.1 as optically measured in separate experiments. The interference patterns in figure 3 allow us to estimate the film thickness in the thinning region (Isenberg 1992; van der Veen *et al.* 2012), which ranges from 50 to 200 nm. Thus, we take 10^2 nm as a characteristic scale of h_t , a value consistent with the thickness of a thinning region that appears when a surfactant spreads on a liquid film (Jensen & Grotberg 1992).

Balancing the driving force $\Delta\gamma$ and the resisting force F_r leads to a scaling law for r_b given by

$$r_b \sim \sqrt{\frac{\gamma_0 a \theta_b}{\mu \ln(\Lambda/h_t)}} t^{1/2}. \quad (3.1)$$

We compare the theory with our experimental measurement results of r_b for different liquids, original film thickness and source locations in figure 5. Here we take $\Lambda = 3 \text{ mm}$, an empirical value which hardly changes in the course of dewetting regardless of experimental conditions. Slight variations of Λ/h_t have negligible effects on its logarithmic value and the scaling result. We see that the raw data, which are scattered in figure 5(a), are collapsed onto a single line when plotted according to (3.1) in figure 5(b). The slope of the best fitting line is 0.36. We note that the bulk rim was also reported to recede with its inner radius growing like $t^{1/2}$ when a liquid alcohol, instead of vapour, was continuously supplied at a localized spot on a water film (Hernández-Sánchez *et al.* 2015).

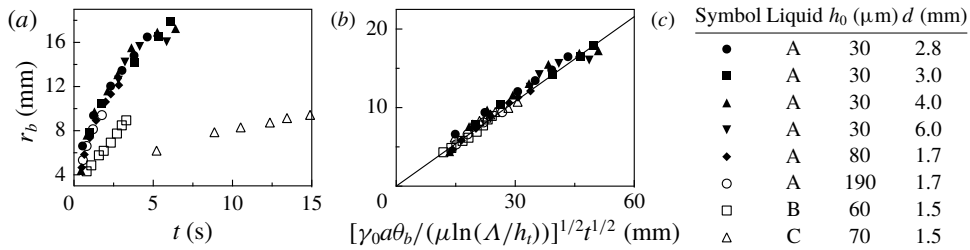


FIGURE 5. (a) Experimentally measured inner radius of bulk film r_b versus time t . (b) r_b plotted according to the scaling law (3.1). (c) Experimental conditions for the symbols.

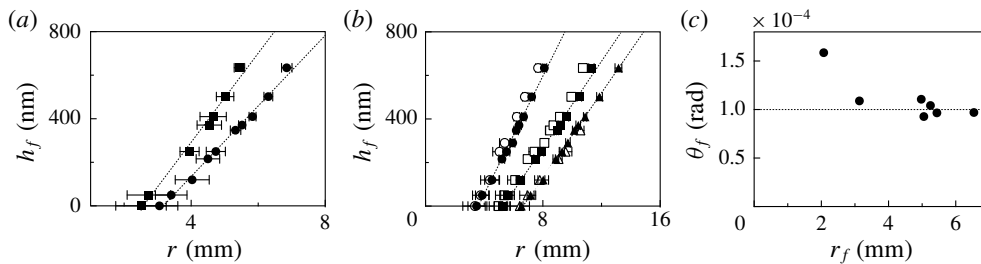


FIGURE 6. (a) Experimentally measured thickness profiles of the fringe film at $t = 1.8$ s under different source distances, $d = 1.6$ (circles) and 3.3 mm (squares). (b) Thickness profiles of the dewetting fringe film. Circles, squares and triangles correspond to the measured height at $t - t_d = 2.2, 5.0$ and 7.4 s, respectively. The filled and empty symbols are for $d = 1.6$ and 3.3 mm, respectively. (c) The receding contact angle of the fringe film θ_f versus r_f . The liquid is water and the original film thickness $h_0 = 30$ μm .

3.2. Receding of fringe film

The inner radius of the fringe film, r_f , matters when the centre is completely dried to result in hole nucleation. The annular fringe spacings of interference patterns, which are evident in figure 3, allow us to construct the thickness profile near the contact line as shown in figure 6. Figure 6(a) shows that the locations of the contact line, or r_f , differ even at the same t depending on the distance of the source d . It is because of a delay time, t_d , before the hole nucleates, which is a function of d : $t_d = 0.2$ and 1.0 s for $d = 1.6$ and 3.3 mm, respectively. When we plot the thickness profiles under different source distances d at the same time after nucleation, $t - t_d$, they coincide as shown in figure 6(b). The slopes of the trend lines in figures 6(a) and 6(b) give the receding contact angles of the fringe film, θ_f , as a function of r_f . Figure 6(c) shows that θ_f is almost constant except for the extremely early stages of the hole nucleation.

The growth of the hole can be driven either by the surface tension effects or the evaporation. We first check whether the Marangoni effects that worked for the aforementioned bulk receding play an important role. Balancing the difference of the liquid–gas interfacial tension across the fringe film (from r_f to r_i), $\Delta\gamma \sim 10^{-2}$ N m^{-1} , with the viscous resisting force in the wedge-like fringe film per unit depth, $F_r \sim \mu \dot{r}_f \ln[(r_i - r_f)/\lambda]/\theta_f$, gives $\dot{r}_f \sim \Delta\gamma\theta_f/[\mu \ln[(r_i - r_f)/\lambda]]$. Here, λ is the cut-off distance of molecular length scale, which is introduced to relieve the singularity at the contact line (de Gennes 1985). Considering that λ ranges from 1 to 10 nm, typical for highly wettable smooth surfaces (Bonaccorso, Kappl & Butt 2002; Cheng

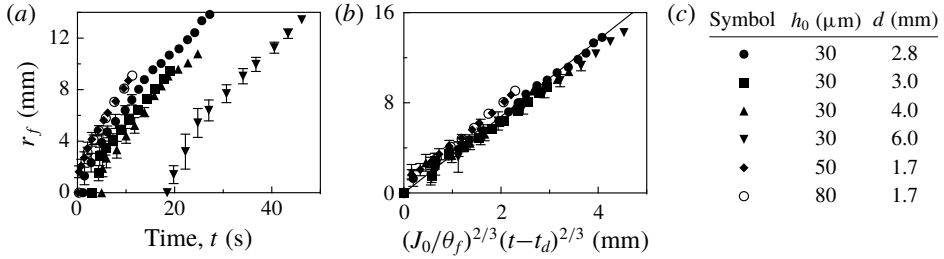


FIGURE 7. (a) Experimentally measured inner radius of the fringe film r_f versus time t . (b) r_f plotted according to the scaling law (3.2). The slope of the best fitting line is 3.4. (c) Experimental conditions for the water films.

& Giordano 2002; Joseph & Tabeling 2005), and that $r_t - r_f \sim 1$ mm, we find $\dot{r}_f \sim 10^{-5}$ m s $^{-1}$, which is much lower than the observed dewetting velocity of the fringe film ($\sim 10^{-3}$ m s $^{-1}$).

We thus turn to the effects of evaporation on the dewetting of fringe film. The steady diffusion equation from the liquid interface to the air gives the volume evaporation rate per unit area near the contact line, $J = J_0 x^{-(\pi/2 - \theta_f)/(\pi - \theta_f)}$, where x is the distance from the contact line, $x = r - r_f$ (Deegan *et al.* 1997). For $\theta_f \ll 1$, we get $J \approx J_0/\sqrt{x}$ with J_0 , a function of the diffusivity and the saturation concentration of the liquid molecules in the air and a typical length scale of the fringe film, being estimated to be $J_0 \sim 10^{-9}$ m $^{3/2}$ s $^{-1}$ (Berteloot *et al.* 2008). Balancing the rate of volume evaporation per unit depth with the rate of wedge disappearance, we write $\int_0^{r_f} J_0/\sqrt{x} dx \sim d(r_f^2 \theta_f)/dt$, which leads to $dr_f/dt \sim (J_0/\theta_f)r_f^{-1/2}$. Because the radius of a hole increases from zero to r_f for the duration of $t - t_d$, we finally obtain

$$r_f \sim \left(\frac{J_0}{\theta_f} \right)^{2/3} (t - t_d)^{2/3}. \quad (3.2)$$

With typical measured values of $\theta_f \sim 10^{-4}$ and $r_f \sim 10^{-3}$ m, \dot{r}_f is estimated to be of the order of 10^{-3} m s $^{-1}$, consistent with the experimental results shown in figure 7(a). When plotting the scattered raw data obtained for different original film thickness and source distances according to the scaling law (3.2), they are collapsed onto a single line as shown in figure 7(b). Therefore, we see that the dewetting of fringe film is caused primarily by evaporation rather than the Marangoni effects. A similar power law for the receding distance of the contact line, which depends on $t^{2/3}$, was reported previously when a sessile drop dries while leaving a band of suspension particles at its periphery (Rio *et al.* 2006; Berteloot *et al.* 2012).

3.3. Creation of thinning region

The thinning region, located between the IPA-rich fringe film and the IPA-poor bulk film, has a very small thickness as shown in figure 4(a). Figure 8(a) shows that the experimentally measured onset radius of the thinning region, $r_{t,0}$, decreases with h_0 . That is, the larger the original film thickness, the earlier the thinning region appears. Furthermore, we see in figure 8(a) that it emerges earlier for a less viscous liquid (liquid A, filled symbols). The film thickness is reduced in the thinning region because too much liquid is drawn into the bulk. We attribute this flow to excessively

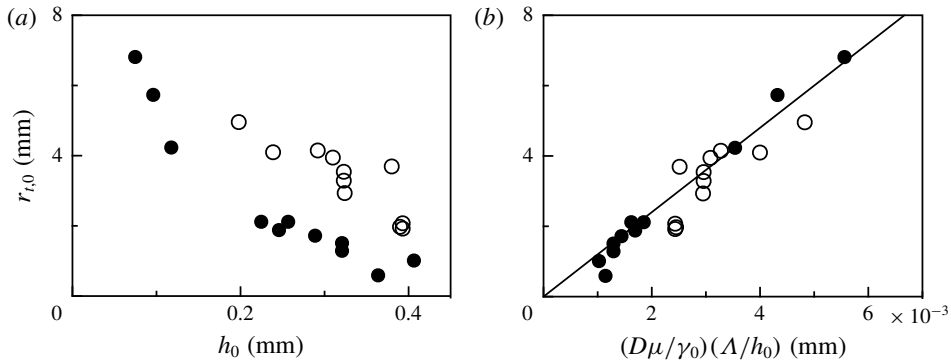


FIGURE 8. (a) Experimentally measured inner radius of thinning region at its onset, $r_{t,0}$, versus the original film thickness h_0 . (b) Measurement values of $r_{t,0}$ plotted according to the scaling law (3.3). The slope of the best fitting line is 1200. Filled and empty symbols correspond to liquid A and B, respectively.

large Marangoni forces along the same line as Gaver & Grotberg (1990, 1992) and Warner *et al.* (2004), which considered a thinning region arising from spreading of a surfactant drop on a thin liquid film.

When the thinning region emerges, the imbalance of IPA concentrations of the liquid surface within and beyond the radius $r_{t,0}$ occurs, which allows us to obtain a scaling law for $r_{t,0}$ as a function of h_0 and the material properties. IPA molecules are supplied from the source by diffusion in the air, and the IPA concentration on the liquid surface at the radius r is estimated as $c/c_s \approx a/r$ in § 3.1. The supply rate of IPA to the liquid surface by diffusion, or the diffusion velocity U_d is scaled as $U_d \sim -D\partial(c/c_s)/\partial r \sim Da/r^2$. Those IPA molecules are rapidly carried away by advection into the bulk region, whose velocity U_a is given by the balance between the Marangoni stress and the viscous shear stress, $\Delta\gamma/\Lambda \sim \mu U_a/h_0$. Here, $\Delta\gamma$ corresponds to the difference of the liquid–gas interfacial tension across the ridge over which the driving force for advection acts: $\Delta\gamma \sim \gamma_0 a/r$ as derived in § 3.1. Thus, U_a is scaled as $U_a \sim \gamma_0 a h_0 / (\mu r \Lambda)$.

The thinning region occurs where U_a overwhelms U_d , so that we scale the onset radius of thinning region as

$$r_{t,0} \sim \frac{D\mu}{\gamma_0} \frac{\Lambda}{h_0}. \quad (3.3)$$

Figure 8 shows that the scattered raw data of the onset radius of the thinning region in (a) are collapsed onto a single line in (b) when plotted according to the scaling law (3.3). It implies that for greater h_0 and lower μ , advection of IPA becomes stronger as compared with diffusion, resulting in an earlier appearance of the thinning region. The slope of the best fitting line in figure 8(b) corresponds to the Péclet number, $Pe = U_a/U_d = 1200$, a ratio of IPA advection rate in liquid to IPA diffusion rate in air.

4. Conclusions

We have shown that a thin liquid film on a highly wettable solid can be dewetted by the vapour-mediated Marangoni effect when a liquid drop of a relatively low surface

tension is placed nearby. The separate measurement of instantaneous liquid–gas interfacial tension depending on the surrounding IPA vapour concentration gave the Marangoni stress as a function of the distance from the source, which played a pivotal role in constructing scaling laws for the dewetting dynamics. The dynamics of three important length scales, inner radii of bulk film, thinning region and fringe film, that define the liquid film morphology have been analysed through scaling analysis. It is interesting to note that although their evolutions occur simultaneously, different forces or mechanisms are at work to generate each region. The recession of bulk is driven by the Marangoni force while resisted by the viscous dissipation in the ridge, to give $r_b \sim t^{1/2}$. The fringe film surrounding a dry hole recedes owing to evaporation in the centre, and the associated mass balance leads to $r_f \sim t^{2/3}$. The thinning region appears where the Marangoni advection velocity of liquid overwhelms the diffusion rate of IPA vapour in the air, to give $r_{t,0} \sim h_0^{-1}$.

Evolution of each length scale is essential in sophisticated control of liquid film dynamics. The inner radius of bulk corresponds to the entire range where the liquid is disturbed by IPA vapour. The inner radius of fringe film gives the area of the dry hole, the most salient feature in the film dewetting. The thinning region beyond the fringe film is also prone to complete drying owing to its small thickness, potentially allowing us to generate multiple dry spots with a single drop of alcohol.

Although we have focused on thin films where the fringe, bulk and thinning region develop distinctively, their discrimination may become hardly possible as the film thickness increases. As shown in figure 8(b), the thinning region appears so early that the fringe can seldom grow for very thick films. The high concentration of IPA near the centre may expedite evaporation of the thinning region, facilitating the hole nucleation. Another aspect which calls for further study is a role of solid–gas interfacial tension change in the hole growth owing to surrounding IPA vapour. While we have precluded such effects in modelling r_f of thin films based on the insignificant change of the receding dynamic contact angle θ_f , the detailed study of the solid surface energy under the vapour-mediated Marangoni effect may further our understanding of the aforementioned droplet movement as well as the dewetting of thick films.

The vapour-mediated scheme to control liquid surfaces hardly alters the volumetric properties of the liquid when the exposure time to vapour is short. Even the surface tension is restored to its original value after removing alcohol vapour. It is particularly relevant to such semiconductor manufacturing processes as rinsing (Kern 1990), cleaning (Reinhardt & Kern 2018) and drying (Mishima *et al.* 1989; Leenaars *et al.* 1990), where elimination of contaminants is critical. Furthermore, the scheme can be used even when the alcohol source and the interface are separated by porous barriers like membranes (Jin *et al.* 2012), extending our capability to remotely control fluid flows in a variety of circumstances.

Acknowledgements

This work was supported by National Research Foundation of Korea (grant no. 2018-052541) and Korea Health Industry Development Institute, Ministry of Health & Welfare (grant no. HI18C0432) via SNU-IAMD.

Appendix A. Effects of IPA vapour on surface tension change of aqueous liquids

Here we briefly discuss the implications of our experimental observations of the surface tension change of aqueous liquids owing to IPA vapour in the surrounding

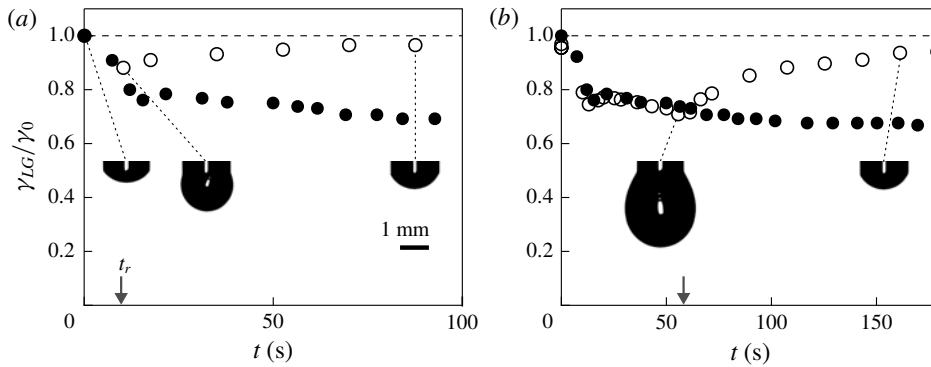


FIGURE 9. The temporal evolution of the surface tension coefficient of a pendant water drop with $s = 20$ mm and $l = 37$ mm. The filled symbols correspond to the continual supply of IPA vapour from the source as shown in figure 1(a). The open symbols are for the experiment where IPA vapour is suddenly removed. The removal occurs at (a) $t_r = 10$ s in phase I and (b) $t_r = 60$ s in phase II.

air. We are focused on the physical reasoning behind the observed phenomena, rather than rigorous theoretical development of such novel dynamic surface tension, which calls for a significant amount of future work. Figure 2(b) exhibits two distinct regimes in the temporal evolution of γ_{LG} , of which phase I is our primary interest because it is relevant to the film dewetting process. But we include the physical reasoning for phase II as well, which may help us to understand the mechanism working in phase I more clearly.

Figure 9 shows the effects of the removal of IPA vapour on the temporal evolution of γ_{LG} . As mentioned in § 2.1, the surface tension coefficient is recovered following the removal of IPA vapour, as shown in figure 9. The results suggest the following physical picture for surface tension change.

If the bulk mixing of IPA with water is responsible for the change of the surface tension, the surface tension values measured for a duration of t_r under the supply of IPA vapour correspond roughly to those of the concentration boundary layer, which reaches the thickness of $\delta \sim (D_1 t_r)^{1/2}$. Here the diffusivity of IPA in water $D_1 \sim 10^{-9}$ m² s⁻¹, and $t_r = 10$ and 60 s in figures 9(a) and 9(b), respectively. In the absence of IPA vapour in air after time t_r , the IPA concentration in the boundary layer formed within the spherical periphery should be smoothed out owing to diffusion into the bulk. The diffusion time scale for such smoothing can be scaled as $\tau_b \sim R^2/D_1 \sim 10^3$ s with $R \sim 10^{-3}$ m being the characteristic radius of the pendant drop, which is too far from the recovery time scale seen in figure 9.

The change of γ_{LG} is then modelled to be caused by the surface concentration of IPA, c^* , which results from a balance between the adsorption rate from the gas phase and the absorption rate into the liquid bulk. Then c^* , with the unit of g m⁻², is estimated to follow $\partial c^*/\partial t = J_d - J_b$. Here J_d is the net adsorption rate of IPA from the surrounding gas to unit area of liquid surface, whose magnitude is proportional to c (Sutherland 1952; Miller, Joos & Fainerman 1994). Here J_b is the net absorption rate of IPA into the liquid bulk from unit interfacial area, proportional to c^* when the bulk concentration of IPA is negligible (Baret 1968; Dukhin, Kretzschmar & Miller 1995). Combining the observations of γ_{LG} in phase I of figure 2(b) and figure 9(a) leads us to speculate that the adsorption (J_d) dominates over the absorption (J_b) in

phase I to sustain a continual decrease of γ_{LG} . The adsorption of soluble molecules at the liquid–gas interface is known to occur at a layer of molecular thickness, so-called subsurface (Eastoe & Dalton 2000). It is likely that hydrophilic hydroxyl groups of IPA make contact with the water surface while hydrophobic alkyl groups stay in the air to avoid water, achieving a molecular arrangement similar to that of surfactant monomers (Shaw 1992). Owing to the dominant effect of the adsorption governed by the instantaneous IPA vapour concentration, c , the somewhat scattered data of figure 2(b), measured for different times and distances from the source, are collapsed onto a single curve when γ_{LG}/γ_0 is plotted versus c/c_s in figure 2(c).

The plateauing behaviour of γ_{LG}/γ_0 in phase II of figure 2(b) is supposed to be caused by the following two facts. First, IPA is highly surface active (Vázquez, Alvarez & Navaza 1995), which results in a rapid decrease of γ_{LG} with a small amount of IPA vapour initially but rather a mild decrease of γ_{LG} afterwards. Second, for low concentration of IPA in liquid, the equilibrium molar fraction of IPA in air is much higher than in the liquid (Brunjes & Bogart 1943). Furthermore, the steep increase of IPA concentration in air causes only a slight increase of IPA concentration in the liquid. In phase II, therefore, IPA concentration in the subsurface is expected to hardly change despite continued growth of c/c_s in air.

Now we discuss the estimation of γ_{LG} in our dewetting experiments. The original film thickness ranging from ~ 10 to $100 \mu\text{m}$ is similar to the concentration boundary layer thickness in figure 9(a), whose surface tension is governed by the adsorption of IPA rather than the bulk mixing. In our model, the difference of the liquid–gas interfacial tension from the inner edge of the ridge to the outer plateau is estimated as $\Delta\gamma/\gamma_0 \sim c/c_s \sim a/r$ in § 3.1. Because the fresh surface is continually generated as the bulk recedes, the instantaneous value of the interfacial tension upon the surface generation at the inner edge of the bulk is likely to be dominated by adsorption of IPA molecules in air with the concentration of c . Then the volumetric composition of IPA, c_b , can be increased through absorption with time. Obtaining the temporal evolution of c_b in the inner edge of the bulk needs consideration of the replenishing influx of uncontaminated liquid from the bulk as well as the diffusive transport of IPA into the neighbouring bulk and the film, a topic that requires complicated further analysis. Here we assume the dominant effects of c on γ_{LG} associated with the vigorous adsorption of IPA to the continually generated fresh liquid surface in the inner edge of the bulk owing to the low concentration of IPA vapour in air during the dewetting experiments ($c/c_s < 0.15$).

REFERENCES

- BANGHAM, D. H. & SAWERIS, Z. 1938 The behaviour of liquid drops and adsorbed films at cleavage surfaces of mica. *Trans. Faraday Soc.* **34**, 554–570.
- BARET, J. F. 1968 Kinetics of adsorption from a solution. Role of the diffusion and of the adsorption-desorption antagonism. *J. Phys. Chem.* **72**, 2755–2758.
- BATCHELOR, G. K. 1967 *An Introduction to Fluid Dynamics*. Cambridge University Press.
- BERENDSEN, C. W. J., ZEEGERS, J. C. H., KRUIS, G. C. F. L., RIEPEN, M. & DARHUBER, A. A. 2012 Rupture of thin liquid films induced by impinging air-jets. *Langmuir* **28**, 9977–9985.
- BERG, S. 2009 Marangoni-driven spreading along liquid–liquid interfaces. *Phys. Fluids* **21**, 032105.
- BERTELOOT, G., HOANG, A., DAERR, A., KAVEHPOUR, H. P., LEQUEUX, F. & LIMAT, L. 2012 Evaporation of a sessile droplet: inside the coffee stain. *J. Colloid Interface Sci.* **370**, 155–161.
- BERTELOOT, G., PHAM, C.-T., DAERR, A., LEQUEUX, F. & LIMAT, L. 2008 Evaporation-induced flow near a contact line: consequences on coating and contact angle. *Europhys. Lett.* **83**, 14003.

- BONACCURSO, E., KAPPL, M. & BUTT, H.-J. 2002 Hydrodynamic force measurements: boundary slip of water on hydrophilic surfaces and electrokinetic effects. *Phys. Rev. Lett.* **88**, 076103.
- BRUNJES, A. S. & BOGART, M. J. P. 1943 Vapor-liquid equilibria for commercially important systems of organic solvents: the binary systems ethanol-n-butanol, acetone-water and isopropanol-water. *Ind. Engng Chem.* **35**, 255–260.
- BUTT, J. B., GRAF, K. & KAPPL, M. 2006 *Physics and Chemistry of Interfaces*. Wiley.
- CARLES, P. & CAZABAT, A. M. 1989 Spreading involving the Marangoni effect: some preliminary results. *Colloids Surf.* **41**, 97–105.
- CARSLAW, H. S. & JAEGER, J. C. 1959 *Conduction of Heat in Solids*. Clarendon Press.
- CHENG, J.-T. & GIORDANO, N. 2002 Fluid flow through nanometer-scale channels. *Phys. Rev. E* **65**, 031206.
- CIRA, N. J., BENUSIGLIO, A. & PRAKASH, M. 2015 Vapour-mediated sensing and motility in two-component droplets. *Nature* **519**, 446–450.
- DE GENNES, P. G. 1985 Wetting: statics and dynamics. *Rev. Mod. Phys.* **57**, 827–863.
- DEEGAN, R. D., BAKAJIN, O., DUPONT, T. F., HUBER, G., NAGEL, S. R. & WITTEN, T. A. 1997 Capillary flow as the cause of ring stains from dried liquid drops. *Nature* **389**, 827–829.
- DUKHIN, S. S., KRETZSCHMAR, G. & MILLER, R. 1995 *Dynamics of Adsorption at Liquid Interfaces: Theory, Experiment, Application*. Elsevier.
- EASTOE, J. & DALTON, J. S. 2000 Dynamic surface tension and adsorption mechanisms of surfactants at the air-water interface. *Adv. Colloid Interface Sci.* **85**, 103–144.
- GAVER, D. P. & GROTBORG, J. B. 1990 The dynamics of a localized surfactant on a thin film. *J. Fluid Mech.* **213**, 127–148.
- GAVER, D. P. & GROTBORG, J. B. 1992 Droplet spreading on a thin viscous film. *J. Fluid Mech.* **235**, 399–414.
- HERNÁNDEZ-SÁNCHEZ, J. H., EDDI, A. & SNOEIJER, J. H. 2015 Marangoni spreading due to a localized alcohol supply on a thin water film. *Phys. Fluids* **27**, 032003.
- ISENBERG, C. 1992 *The Science of Soap Films and Soap Bubbles*. Dover.
- JENSEN, O. E. & GROTBORG, J. B. 1992 Insoluble surfactant spreading on a thin viscous film: shock evolution and film rupture. *J. Fluid Mech.* **240**, 259–288.
- JIN, H., MARMUR, A., IKKALA, O. & RAS, R. H. A. 2012 Vapour-driven Marangoni propulsion: continuous, prolonged and tunable motion. *Chem. Sci.* **3**, 2526–2529.
- JOSEPH, P. & TABELING, P. 2005 Direct measurement of the apparent slip length. *Phys. Rev. E* **71**, 035303.
- KEISER, L., BENSE, H., COLINET, P., BICO, J. & REYSSAT, E. 2017 Marangoni bursting: evaporation-induced emulsification of binary mixtures on a liquid layer. *Phys. Rev. Lett.* **118**, 074504.
- KELLER, J. B. 1983 Breaking of liquid films and threads. *Phys. Fluids* **26**, 3451–3453.
- KERN, W. 1990 The evolution of silicon wafer cleaning technology. *J. Electrochem. Soc.* **137**, 1887–1892.
- KIM, H.-Y., LEE, H. J. & KANG, B. H. 2002 Sliding of liquid drops down an inclined solid surface. *J. Colloid Interface Sci.* **247**, 372–380.
- KIM, H.-Y. 2007 On thermocapillary propulsion of microliquid slug. *Nanoscale Microscale Thermophys. Engng* **11**, 351–362.
- KIM, H., MULLER, K., SHARDT, O., AFKHAMI, S. & STONE, H. A. 2017 Solutal Marangoni flows of miscible liquids drive transport without surface contamination. *Nat. Phys.* **13**, 1105–1110.
- KIM, S., MOON, M.-W. & KIM, H.-Y. 2013 Drop impact on super-wettability-contrast annular patterns. *J. Fluid Mech.* **730**, 328–342.
- LEENAARS, A. F. M., HUETHORST, J. A. M. & VAN OEKEL, J. J. 1990 Marangoni drying: a new extremely clean drying process. *Langmuir* **6**, 1701–1703.
- LUGG, G. A. 1968 Diffusion coefficients of some organic and other vapors in air. *Anal. Chem.* **40**, 1072–1077.
- MARRA, J. & HUETHORST, J. A. M. 1991 Physical principles of Marangoni drying. *Langmuir* **7**, 2748–2755.
- MATAR, O. K. & CRASTER, R. V. 2001 Models for Marangoni drying. *Phys. Fluids* **13**, 1869–1883.

- MILLER, R., JOOS, P. & FAINERMAN, V. B. 1994 Dynamic surface and interfacial tensions of surfactant and polymer solutions. *Adv. Colloid Interface Sci.* **49**, 249–302.
- MISHIMA, H., YASUI, T., MIZUNIWA, T., ABE, M. & OHMI, T. 1989 Particle-free wafer cleaning and drying technology. *IEEE Trans. Semicond.* **2**, 69–75.
- REDON, C., BROCHARD-WYART, F. & RONDELEZ, F. 1991 Dynamics of dewetting. *Phys. Rev. Lett.* **66**, 715–718.
- REINHARDT, K. & KERN, W. 2018 *Handbook of Silicon Wafer Cleaning Technology*. William Andrew.
- RIO, E., DAERR, A., LEQUEUX, F. & LIMAT, L. 2006 Moving contact lines of a colloidal suspension in the presence of drying. *Langmuir* **22**, 3186–3191.
- SHAW, D. J. 1992 *Introduction to Colloid and Surface Chemistry*, 4th edn. Butterworth-Heinemann.
- SUTHERLAND, K. L. 1952 The kinetics of adsorption at liquid surfaces. *Aust. J. Sci. Res. A* **5**, 683–696.
- TROIAN, S. M., HERBOLZHEIMER, E. & SAFRAN, S. A. 1990 Model for the fingering instability of spreading surfactant drops. *Phys. Rev. Lett.* **65**, 333–336.
- VAN DER VEEN, R. C. A., TRAN, T., LOHSE, D. & SUN, C. 2012 Direct measurements of air layer profiles under impacting droplets using high-speed color interferometry. *Phys. Rev. E* **85**, 026315.
- VÁZQUEZ, G., ALVAREZ, E. & NAVAZA, J. M. 1995 Surface tension of alcohol + water from 20 to 50 °C. *J. Chem. Engng Data* **40**, 611–614.
- WARNER, M. R. E., CRASTER, R. V. & MATAR, O. K. 2004 Fingering phenomena associated with insoluble surfactant spreading on thin liquid films. *J. Fluid Mech.* **510**, 169–200.